OXFORD

ORIGINAL ARTICLE

Fast-spiking Parvalbumin Interneurons are Frequently Myelinated in the Cerebral Cortex of Mice and Humans

J. Stedehouder[1], J. J. Couey[1], D. Brizee[1], B. Hosseini[1], J. A. Slotman[2,3], C. M. F. Dirven[4], G. Shpak[1], A. B. Houtsmuller[2,3] and S. A. Kushner[1]

[1]Department of Psychiatry, Erasmus MC, 3000 CA Rotterdam, The Netherlands, [2]Erasmus Optical Imaging Centre, Erasmus University Medical Center, 3000 CA Rotterdam, The Netherlands, [3]Department of Pathology, Erasmus MC, 3000 CA Rotterdam, The Netherlands and [4]Department of Neurosurgery, Erasmus MC, 3000 CA Rotterdam, The Netherlands

Address correspondence to S. A. Kushner. Email: s.kushner@erasmusmc.nl

Abstract

Myelination, the insulating ensheathment of axons by oligodendrocytes, is thought to both optimize signal propagation and provide metabolic support. Despite the well-established physiological importance of myelination to neuronal function, relatively little is known about the myelination of GABAergic interneurons in the cerebral cortex. Here, we report that a large fraction of myelin in mouse cerebral cortex ensheaths GABAergic interneurons, reaching up to 80% in hippocampal subregions. Moreover, we find that a very high proportion of neocortical and hippocampal parvalbumin (PV) interneurons exhibit axonal myelination. Using a combination of intracellular recordings and biocytin labeling of ex vivo human neocortex, we also confirm that axons of fast-spiking PV interneurons are extensively myelinated in the human brain. PV interneuron myelination in both mice and humans exhibits a stereotyped topography with a bias towards proximal axonal segments and relatively short internodes (~27 μm) interspersed with branch points. Interestingly, myelin-deficient *Shiverer* mice exhibit an increased density and more proximal location of en passant boutons, suggesting that myelination might function in part to regulate synapse formation along PV interneuron axons. Taken together, fast-spiking interneuron myelination is likely to have broad implications for cerebral cortex function in health and disease.

Key words: interneuron, myelination, parvalbumin, human, mouse, cerebral cortex

Introduction

Myelination is the insulating ensheathment of axons by oligodendrocytes, demonstrated to optimize action potential (AP) propagation and metabolic demands (Lee et al. 2012b; Nave and Werner 2014; Saab et al. 2016). Axonal myelination has recently been shown to be modulated by neuronal activity (Gibson et al. 2014) and social experience (Liu et al. 2012; Makinodan et al. 2012), and impaired in several psychiatric disorders including schizophrenia, bipolar disorder, and autism spectrum disorder (Barysheva et al. 2013; White et al. 2013; Kumar et al. 2015; Rane et al. 2015).

In the cerebral cortex, the myelination of pyramidal neurons has been extensively investigated (Tomassy et al. 2014), but comparatively little is known about myelination of GABAergic interneurons. Several studies have reported myelination of local GABAergic interneurons throughout the brain (McGee et al. 2005; Micheva et al. 2016; Stedehouder and Kushner 2017). However, the ubiquity of cerebral cortex parvalbumin-positive (PV[+]) interneuron myelination remains largely unexplored in mice, and has rarely been investigated in humans.

GABAergic interneurons exert a powerful modulation on local cerebral cortex network activity and brain oscillations. In particular,

the fast-spiking, PV$^+$ subclass of interneurons functions crucially in governing feedforward and feedback inhibition in cortical microcircuits, as well as tightly regulating fast network oscillations (Hu and Jonas 2014). Dysfunction of PV$^+$ interneuron function has been strongly linked to multiple psychiatric disorders (Marín 2012).

In the current study, we examined the myelination of GABAergic interneurons in the cerebral cortex of mice and humans. Using cell-type specific fluorescent reporter lines, we found that a substantial fraction of myelin in the cortex and hippocampus belongs to GABAergic interneurons, in particular fast-spiking PV$^+$ interneurons. Using viral labeling, the vast majority of PV$^+$ interneurons we examined in the cortex and hippocampus exhibited myelinated axons. Furthermore, we independently replicated this finding in both mouse and human cerebral cortex using intracellular biocytin labeling during patch-clamp recordings followed by axonal reconstructions. PV$^+$ interneuron myelination exhibited a topography biased towards proximal axonal segments interspersed by unmyelinated branch points. Local axonal morphology was correlated with myelination status, in which interbranch point distances tended to be shorter when the corresponding axonal segment was unmyelinated. Additionally, myelin-deficient *Shiverer* mice exhibited an increased density of proximal en passant boutons, suggesting that myelination functions to regulate the axonal morphology of PV$^+$ interneurons in the cerebral cortex.

Methods

Mice

All experiments were approved by the Dutch Ethical Committee and in accordance with the Institutional Animal Care and Use Committee (IACUC) guidelines. All mouse lines were obtained from Jackson Laboratory:

> *Pvalb*$^{tm1(cre)Arbr}$/J mice (PV::cre) (Hippenmeyer et al. 2005) www.jax.org/strain/008069
> *Sst*$^{tm2.1(cre)Zjh}$/J (SOM::cre) (Taniguchi et al. 2011) www.jax.org/strain/013044
> *Gad2*$^{tm2(cre)Zjh}$/J (GAD2::cre) (Madisen et al. 2012) www.jax.org/strain/010802
> *Gt(ROSA)26Sor*$^{tm14(CAG-tdTomato)Hze}$/J (Ai14) (Madisen et al. 2012) www.jax.org/strain/007908
> *B6;C3Fe.SWV-Mbp*^{shi}/J (Shiv) (Chernoff 1981) www.jax.org/strain/001428
> C57BL/6J (WT) www.jax.org/strain/000664

All lines were backcrossed for more than 10 generations in C57BL/6J. Lines were crossed to obtain heterozygous *PV*::cre x Ai14 (PV::cre;Ai14), SOM::cre x Ai14 (SOM::cre;Ai14), and GAD2::cre x Ai14 mice (GAD2::cre;Ai14). Heterozygous B6;C3Fe.SWV-Mbp^{shi} mice were crossed to obtain homozygous *Shiverer* mice and wild-type littermates. For global myelination quantifications and viral labeling, mice were used from 8 to 12 weeks of age. For electrophysiological recordings, mice were used from 5 to 8 weeks of age. Mice were group-housed and maintained on a 12 h light/dark cycle with ad libitum access to food and water.

Human Brain Tissue

Neocortical tissue was obtained from 3 patients undergoing tumor resection surgery at the Department of Neurosurgery (Erasmus University Medical Center, Rotterdam, The Netherlands). All procedures regarding human tissue were performed with the approval of the Medical Ethical Committee of the Erasmus University Medical Center. Written informed consent of each patient was provided in accordance with the Helsinki Declaration.

Patient #1 was a 54-year-old female presenting with a WHO grade 4 glioblastoma in the right temporo-occipital lobe. She had no significant psychiatric or past medical history, and no history of epilepsy or seizures. Patient received no antiepileptic or cytostatic medication.

Patient #2 was a 69-year-old male presenting with a hemangiopericytoma/solitary fibrous tumor on the posterior border of the left lateral ventricle. He had no significant psychiatric or past medical history, and no history of epilepsy or seizures. Patient received no antiepileptic or cytostatic medication.

Patient #3 was a 59-year-old male presenting with a WHO grade 4 glioblastoma in the right temporal lobe. His psychiatric history was notably only for a single episode of depression which fully remitted and required no maintenance treatment. He had no history of epilepsy, but experienced a single tonic–clonic seizure 3 weeks prior to surgery, for which he was subsequently treated with sodium valproate (1000 mg daily). Patient received no cytostatic medication.

Mouse Viral Labeling

Heterozygous *PV*::cre mice were used for viral-mediated cell-type specific labeling, which was performed using cre-dependent adeno-associated virus (AAV) expression with AAV5/EF1a-DIO-mCherry or AAV5/Flex-eGFP (University of Pennsylvania Viral Vector Core). Virus was diluted to ~5 × 10^{11} GC/mL in phosphate-buffered saline (PBS) to achieve sparse labeling.

Anesthesia was induced using 5% isoflurane, and subsequently maintained with 2% isoflurane during surgery. Body temperature was maintained at 37 °C. Bupivacaine hydrochloride (2.5 mg/mL), Rimadyl (50 mg/mL), and Temgesic (0.3 mg/mL) were administered subcutaneously. Mice were placed into the stereotaxic frame (Stoelting) using stub ear bars for head fixation. Longitudinal scalp incision of 1–2 cm length was made to reveal the skull, and a craniotomy was performed overlying the site of injection at the following coordinates (in mm):

> mPFC: +2 bregma, ±0.5 lateral, —2 vertical
> S1: −1 bregma, ±2 lateral, —0.5 vertical
> CA1: −1.5 bregma, ±1 lateral, —1.5 vertical

A borosilicate glass micropipette was slowly lowered to the target site and remained in place for 5 min before the start of injection. Virus injection was controlled by a manual syringe pump (0.5 μL per location, infusion speed 0.05 μL/min). At the conclusion of the injection, the micropipette was maintained in place for another 5 min and then slowly withdrawn. After surgery, mice were allowed to recover for 3–4 weeks before analysis.

Electrophysiology

Mouse Recordings

Anesthesia was induced using 5% isoflurane and mice were transcardially perfused with 20 mL of ice-cold, N-methyl-D-glucamine (NMDG)-based cutting solution containing (in mM): 93 NMDG, 93 HCl, 30 NaHCO$_3$, 25 D-glucose, 20 HEPES, 5 Na-ascorbate, 2 thiourea, 10 MgCl$_2$, 3 Na-pyruvate, 2.5 KCl, 1.25 NaH$_2$PO$_4$, and 0.5 CaCl$_2$ (300 mOsm, pH 7.4) oxygenated with 95% O$_2$/5% CO$_2$ before decapitation. After decapitation, the brain was quickly dissected in the same ice-cold cutting

solution. For each brain region examined, coronal slices (300 μm) were cut with a vibrating slicer (Microm HM 650 V, Thermo Scientific) and incubated in cutting solution at 37 °C for 30 s, followed by oxygenated (95% O_2/5% CO_2) artificial cerebrospinal fluid (aCSF) at 37 °C for 45 min. aCSF contained (in mM) 127 NaCl, 25 $NaHCO_3$, 25 D-glucose, 2.5 KCl, 1.25 NaH_2PO_4, 1.5 $MgSO_4$, and 1.6 $CaCl_2$. Slices were then allowed to recover at room temperature for at least 1 h before recordings.

In *Shiverer* and wildtype mice, interneurons were visualized using infrared differential interference contrast microscopy. In PV::cre;Ai14 mice, PV^+ interneurons were visualized by native tdTomato fluorescence using an RFP filter (Semrock, Rochester, NY, USA). Whole-cell recordings were made using borosilicate glass pipettes (3.5–5.5 MΩ resistance) with intracellular solution containing (in mM) 120 K-gluconate, 10 KCl, 10 HEPES, 10 K-phosphocreatine, 4 ATP-Mg, 0.4 GTP, and 5 mg/mL biocytin (pH was adjusted to 7.4 using KOH, and osmolarity measured 285–290 mOsm).

Recordings were performed in aCSF at near-physiological temperatures (32–33 °C) using HEKA EPC10 quattro amplifiers and Patchmaster software (40 or 200 kHz sampling rates depending on the total recording length to avoid memory limits during acquisition). Series resistance was typically <20 MΩ and fully compensated for bridge balance and capacitance; recordings in which the series resistance exceeded 20 MΩ were not included in the pooled averages. No correction was made for liquid junction potential. Data analysis was performed offline using Igor Pro v6 (Wavemetrics).

Basic physiological characteristics were determined from voltage responses to square-wave current pulses of 500 ms duration, ranging from −100 pA to +300 pA, and delivered in 20 pA intervals. Input resistance was determined by the slope of the linear regression through the voltage-current curve. Single AP characteristics were obtained from the first elicited AP. AP threshold was defined as the inflection point at the foot of the regenerative upstroke. AP amplitude was defined as the voltage difference between the threshold and peak voltage. AP half-width was measured at half of the peak amplitude. AP rise time was quantified as duration from 10% to 90% of the peak amplitude. The fast after-hyperpolarizing potential was measured as the peak hyperpolarizing deflection following AP initiation. AP frequency was determined from a 500 ms square-wave current pulse of +300 pA.

Human Recordings

Ex vivo recordings of human neocortex were performed using tissue requiring surgical resection in order to access the location of the tumor. Immediately following resection, the neocortical tissue block was directly transferred to oxygenated (95% O_2/5% CO_2) ice-cold cutting solution and transported to the electrophysiology laboratory. The time between tissue resection and slicing was always <10 min. Tissue slices were used for electrophysiological recordings only when no infiltrating tumor cells were detectable in the slice. Whole-cell recordings and electrophysiological analyses were performed identically as for mouse tissue.

In total, we recorded from 22 cells (patient #1: 4 cells; patient #2: 14 cells; patient #3: 4 cells), of which 13 cells (patient #1: 3 cells; patient #2: 8 cells; patient #3: 2 cells) were successfully biocytin-filled and reconstructed.

Fluorescence Immunohistochemistry

Mouse Tissue

Deep anesthesia was induced by intraperitoneal injection of pentobarbital, and mice were transcardially perfused with saline followed by 4% paraformaldehyde (PFA). Brains were dissected and postfixed in 4% PFA for 2 h at room temperature. Brains were transferred into 10% sucrose phosphate buffer (PB 0.1 M, pH 7.3) and stored overnight at 4 °C. Embedding was performed in a 12% gelatin/10% sucrose block, with fixation in 10% PFA/30% sucrose solution (PB 0.1 M, pH 7.3) for 2 h at room temperature and immersed in 30% sucrose (PB 0.1 M, pH 7.3) at 4 °C overnight. Forty micrometer coronal and sagittal sections were collected serially (rostral to caudal) using a freezing microtome (Leica; SM 2000R) and stored in 0.1 M PB. Free-floating sections were incubated in sodium citrate (10 mM) at 80 °C for 30 min and rinsed with PBS (pH 7.3). Sections were preincubated with a blocking PBS buffer containing 0.5% Triton X-100 and 10% normal horse serum (NHS; Invitrogen) for 1 h at room temperature. Sections were incubated in a mixture of primary antibodies in PBS buffer containing 0.4% Triton X-100 and 2% NHS for 72 h at 4 °C.

The following primary antibodies were used: rabbit anti-mCherry (1:500, Millipore, Abcam, ab167453), mouse anti-PV (1:1000, Swant, 235), and goat anti-MBP (1:300, Santa Cruz, C-16, sc-13 914). We additionally confirmed the specificity of the anti-MBP antibody using both western blot analysis and immunofluorescence labeling in tissue from MBP-deficient *Shiverer* mice (Supplementary Fig. 9).

For recovery of biocytin-labeled cells following electrophysiological recordings, slices were incubated overnight at 4 °C in 4% PFA. Slices were then rinsed at room temperature in 0.1 M PB, incubated for 12 h at 4 °C in 10% sucrose (0.1 M PB), and overnight at 4 °C in 30% sucrose (0.1 M PB). Sections were serially recut at 40 μm using a freezing microtome (Leica; SM 2000R) and stored in 0.1 M PB at 4 °C.

Sections were washed with PBS, and incubated with corresponding Alexa-conjugated secondary antibodies (1:300, Invitrogen) and cyanine dyes (1:300, Sanbio) in PBS buffer containing 0.4% Triton X-100, 2% NHS for 2 h at room temperature. For biocytin-labeled cells, streptavidin-A488 (1:300, Jackson) was used. For some experiments, nuclear staining was performed using DAPI (1:10 000, Invitrogen). Sections were washed with PB 0.1 M and mounted on slides, cover slipped with Vectashield H1000 fluorescent mounting medium (Vector Labs) and sealed.

Human Tissue

Three-hundred-micrometer electrophysiology slices were incubated overnight at 4 °C in 4% PFA. Slices were then rinsed at room temperature in 0.1 M PB, incubated for 12 h at 4 °C in 10% sucrose (0.1 M PB), and overnight at 4 °C in 30% sucrose (0.1 M PB). Forty-micrometer sections were collected serially using a freezing microtome (Leica; SM 2000R) and stored in 0.1 M PB. Sections were extensively washed and preincubated with a blocking PBS buffer containing 0.5% Triton X-100 and 5% bovine serum albumin (BSA; Sigma-Aldrich) for 1 h at room temperature. Next, sections were incubated in a mixture of primary antibodies in PBS buffer containing 0.5% Triton X-100 and 1% BSA for 72 h at 4 °C. The following primary antibodies were used: mouse anti-PV (1:1000, Sigma, P3088, clone Parv-19) and goat anti-MBP (1:300, Santa Cruz, C-16, sc-13 914).

Sections were extensively washed with PBS (>2 h), and incubated with corresponding Alexa-conjugated secondary antibodies (1:300, Invitrogen), cyanine dyes (1:300, Sanbio) and streptavidin-A488 (1:300, Jackson) in PBS buffer containing 0.5% Triton X-100 and 1% BSA for 5 h at room temperature. Nuclear staining was performed using DAPI (1:10 000, Invitrogen). Sections were washed with PB 0.1 M and mounted on slides,

cover slipped with Vectashield H1000 fluorescent mounting medium (Vector Labs) and sealed.

Confocal Imaging and Analysis

Confocal imaging was performed using a Zeiss LSM 700 microscope (Carl Zeiss) equipped with Plan-Apochromat 10×/0.45 and 63×/1.4 (oil immersion) objectives. Alexa488, Cy3, Alexa647, and Alexa405 or DAPI were imaged using excitation wavelengths of 488, 555, 639, and 405 nm, respectively.

Quantification of region-dependent myelination was performed in the prelimbic region of the mPFC (bregma: + 2.10 to +1.54 mm), somatosensory cortex layers (bregma: −0.82 to −1.22 mm) and dorsal hippocampal CA1 (bregma: −1.58 to −1.94 mm) by obtaining z-stack images (1064 × 1064 pixels) at 63×magnification (1.4 NA; oil immersion) with 1× digital zoom at a step size of 1 μm. Stacks were randomly sampled across all layers of mPFC, somatosensory cortex and hippocampal CA1 based on DAPI nuclear labeling, using a 100 × 100 μm counting frame. Immunofluorescent colocalization of MBP and tdTomato was manually counted by 2 independent raters (J. S. and D. B.) using NIH ImageJ (version 1.41). Co-localization was defined as the circumferential bordering of a tdTomato-labeled axon by an MBP$^+$ myelin signal. At least 3 z-stacks were analyzed per mouse per region per layer.

Similar to previous reports (Hu et al. 2013; Jiang et al. 2015; Pala and Petersen 2015), a small fraction of cells in the SOM::cre; Ai14 mice (~10%) had expression of PV in medial prefrontal and somatosensory cortex. Due to the difficulty of performing axonal triple colocalizations (MBP/SOM/PV), and the bona fide endogenous coexpression of PV and SOM in hippocampal bistratified and oriens-lacunosum moleculare cells (Müller and Remy 2014), we have reported the corresponding double colocalizations (MBP/SOM and MBP/PV). The MBP/SOM double colocalizations reported in Figure 1 therefore likely represent an overestimation of the actual frequency of SOM$^+$ interneuron axonal myelination.

For analysis of myelination along virus-labeled PV$^+$ axons, overview images were obtained at 10× with 1× digital zoom. Individually labeled cells distributed over layers II-VI in mPFC and S1, and dorsal hippocampal CA1 stratum oriens, pyramidale and radiatum were categorized and examined at 63× with 1× digital zoom to confirm labeling with the PV antibody. Confocal z-stack images (2128 × 2128 pixels) were obtained at 63× magnification with 1× digital zoom at a step size of 2 μm along the full z-axis extent of the section. Axons were identified as the thinnest, smoothest, and most highly branched processes originating from either the soma or primary dendrite. In addition, axons seemed to branch at more obtuse ≥90° angles from one another, often turning back toward the soma, whereas dendrites branched at smaller angles (<90°), continuing along a trajectory away from the soma. PV$^+$ cells were considered to be myelinated when they exhibited at least one myelinated internode. Cells in which the axon exited the slice before 50 μm were excluded from further analysis.

Axonal reconstructions of mouse and human biocytin-filled cells were obtained at 63× magnification (5320 × 5320 pixels) with 1× digital zoom and a step size of 0.5 μm. Pixel dwell was kept at >1.5 μs for optimal subsequent colocalization identification. Images were transferred to Neurolucida 360 software (v2.6; MBF Bioscience) and reconstructed using interactive tracing with the Directional Kernels method. Reconstructed soma, axon and myelin segments were analyzed with Neurolucida Explorer (MBF Bioscience).

The distance to first myelin was defined as the distance along the axon from the soma, or in the case of dendrite-originating axons the distance from the originating dendrite, to the initial point of MBP immunofluorescence. Myelin segments that exited a slice were removed from subsequent analysis. Identification and reconstruction of axonal myelination was performed blind to electrophysiological (fast-spiking vs. non-fast-spiking) and cell-type (PV$^+$ vs. non-PV) identity. No spatial corrections were made for tissue shrinkage.

Structured Illumination Microscopy

Imaging was performed using a Zeiss Elyra PS1 system. 3D-SIM data were acquired using a 63× 1.4NA oil objective. 488, 561, and 642 100 mW diode lasers were used to excite the fluorophores together with, respectively, a BP 495–575 + LP 750, BP 570–650 + LP 75, or LP 655 emission filter. For 3D-SIM imaging, a grating was present in the light path, and modulated in 5 phases and 5 rotations, and multiple z-slices with an interval of 110 nm were recorded on an Andor iXon DU 885, 1002 × 1004 EMCCD camera. Raw images were reconstructed using Zen (Zeiss).

For axonal bouton quantifications, SIM images were obtained from proximal axons of biocytin-filled cells up to the third branch order. En passant bouton density, as well as proximal axonal lengths, were quantified using Neurolucida 360 (v2.6; MBF Bioscience).

Western Blotting

Adult homozygous *Shiverer* mice and WT littermates were anesthetized using isoflurane, sacrificed by decapitation, and snap frozen in liquid nitrogen. Protein lysates were prepared by homogenization of cortical brain samples in lysis buffer (10 mM Tris–HCl pH 6.8, 2.5% SDS, 2 mM EDTA) and adjusted to a concentration of 1 mg/mL. Western blots were probed with primary antibodies against MBP (C-16, sc-13 914, 1:500, Santa Cruz) and β-actin (MAB1501R, 1:10 000, Chemicon), and complementary secondary antibodies (goat anti-mouse and donkey anti-goat, 1:5000, AffiniPure). Blots were imaged using a LI-COR Odyssey Scanner with Odyssey 3.0 software.

Statistical Analysis

Statistical analysis was performed using IBM SPSS (version 21). Sample sizes were chosen based on previous publications utilizing similar methods. Hypothesis testing was performed using unpaired Student's *t*-test or analysis of variance followed by Tukey's post hoc test. All data are expressed as mean ± standard error. Significance threshold was set at $P < 0.05$. Throughout the paper exact P-values values are provided except when $P < 0.001$.

Results

A Substantial Fraction of Cerebral Cortex Myelin Ensheaths PV$^+$ Interneurons

To examine the extent to which GABAergic axons are myelinated in the mouse brain, we utilized the *Ai14* cre-dependent fluorescence reporter strain in combination with cre driver lines for either PV or somatostatin (SOM) interneuron subclasses, or broadly among GABAergic interneurons (Glutamate Decarboxylase 2, GAD65; GAD2). Specifically, we quantified axonal colocalization between the interneuron subclass-specific expression of tdTomato (*Ai14*) and myelin basic protein (MBP) in the medial prefrontal cortex (mPFC), primary somatosensory cortex (S1), and hippocampal CA1 subregion (CA1) using confocal microscopy (Fig. 1a–c, Supplementary Fig. 1) and structured illumination microscopy (SIM; Supplementary Fig. 2, Supplementary
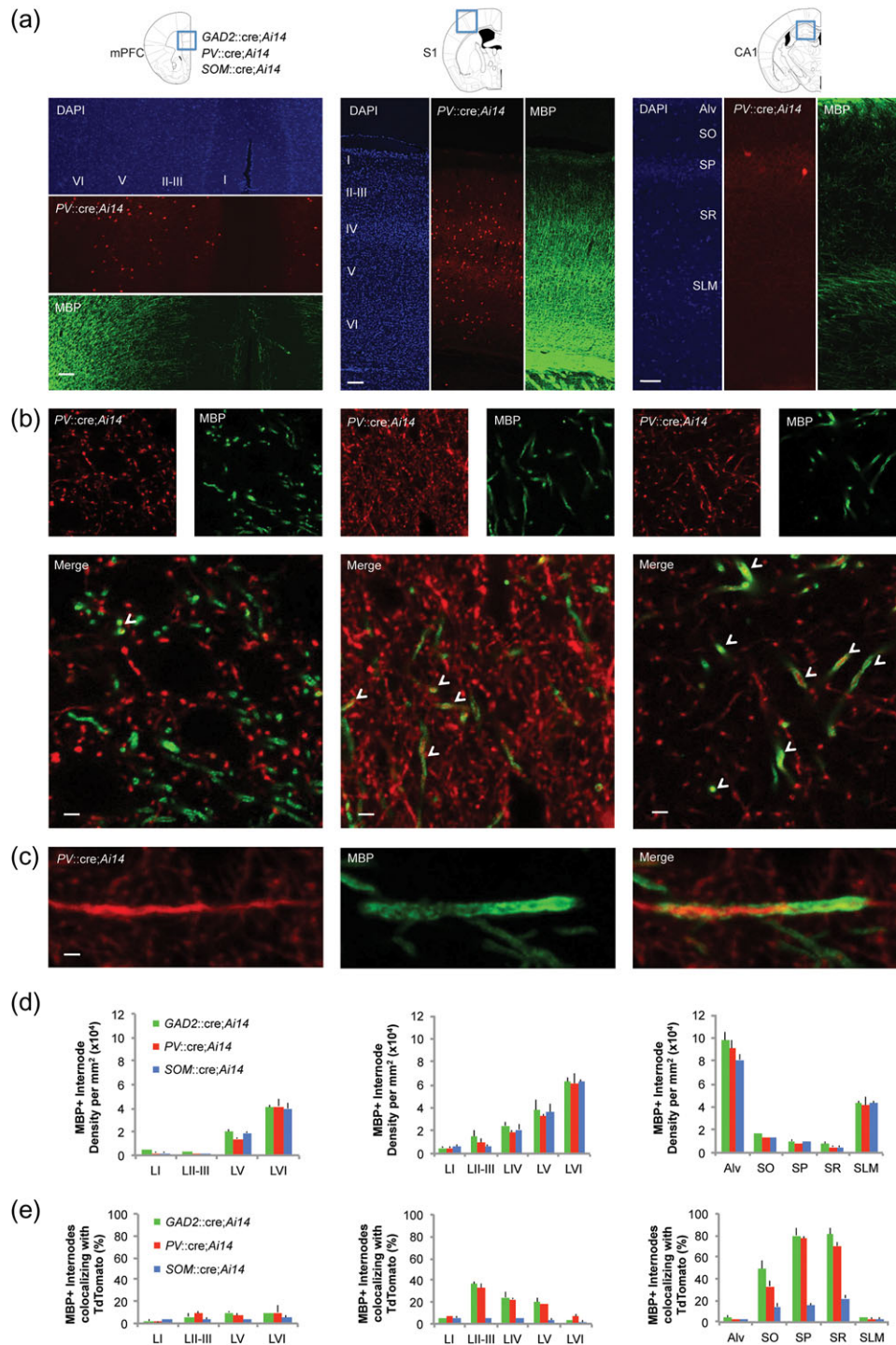
Figure 1. Interneuron myelination is cell-type and region-dependent. (*a*) Representative low-magnification images of *PV*::cre;*Ai14* (red), MBP (green) and DAPI (blue) in the medial prefrontal cortex (mPFC), somatosensory cortex (S1) and hippocampal dorsal CA1 region (CA1). Cell layers are annotated in the DAPI channel. Scale bars for mPFC, S1 and CA1 are 80 µm, 80 µm, and 30 µm, respectively. (*b*) Representative confocal colocalization (arrowheads) between tdTomato (red) and MBP (green) in each respective brain region. Scale bars are 5 µm. (c) Representative colocalization between tdTomato⁺ axon (red) and MBP (green), demonstrating a myelinated axonal segment. Scale bar, 5 µm. (*d*) MBP⁺ internode density varied significantly across cell layers in each brain region examined ($P < 0.001$ for mPFC, S1 and CA1; one-way analyses of variance). In contrast, as expected there were no differences in internode density between *PV*::cre;*Ai14*, *SOM*::cre;*Ai14*, and *GAD2*::cre;*Ai14* reporter lines (repeated measures analysis of variance, Region x Genotype interaction, $P = 0.101$). (*e*) Colocalization of *PV*::cre;*Ai14*, *SOM*::cre;*Ai14*, and *GAD2*::cre;*Ai14* with MBP across cell layers and between regions. Interneuron myelination exhibited a significant Region × Genotype interaction ($P = 0.002$), with main effects of both Region ($P = 0.005$) and Genotype ($P = 0.010$). Post hoc Tukey's test revealed significant differences between PV and SOM myelination in S1 ($P < 0.001$) and CA1 ($P = 0.002$), but not mPFC ($P = 0.722$). $n = 3$ mice per genotype per region. Alv, alveus; SO, stratum oriens; SP, stratum pyramidale; SR, stratum radiatum; SLM, stratum lacunosum moleculare.

Video 1). We observed a systematic gradient of overall myelination across cell layers (Fig. 1d; all regions $P < 0.001$), but importantly without variability of internode density across cre driver lines ($P = 0.101$). Similar to the recent finding of Micheva et al. (Micheva et al. 2016), a sizeable fraction of S1 myelination was attributable to PV$^+$ axons (32.6% in S1 layers II–III) with only a minimal contribution of SOM$^+$ axons or other GAD65$^+$ interneuron subclasses (Fig. 1e). The contribution of PV$^+$ interneuron myelination varied across brain regions ($P = 0.005$), for which the hippocampal CA1 contribution was significantly higher (76.9% in stratum pyramidale) and the mPFC significantly lower (10.1% in layer VI) than in S1 (32.6% in layer II/III). Together, these data confirm that a substantial fraction of cerebral cortex myelin is contributed by PV$^+$ interneurons, albeit with regional variation.

A High Proportion of PV$^+$ Interneurons Exhibit Myelinated Axons

We next asked whether cortical PV$^+$ interneuron myelination is limited to a subset of cells or is more broadly distributed. Sparse labeling of PV$^+$ interneurons was performed using the

PV::cre driver line in combination with stereotactic injections of reduced-titer rAAV5/EF1a-DIO-mCherry virus into mPFC, S1, or CA1 (Fig. 2a). Axons originating from PV$^+$ somata randomly sampled across different layers ($n = 144$; Fig. 2a,b) were examined for MBP immunofluorescence (Fig. 2d). Of the 144 PV$^+$ interneurons examined, 141 (97.9%) exhibited axonal myelination (Fig. 2c). This suggests that cerebral cortex PV$^+$ interneurons are frequently myelinated, independent of cell layer or brain region.

Fast-spiking PV$^+$ Cells Exhibit Region-dependent Proximal Myelination

Next, we addressed the topography of PV$^+$ axonal myelination in order to examine whether internodes are spatially biased along PV$^+$ axons or randomly distributed. We performed whole-cell electrophysiological recordings and intracellular biocytin labeling of fast-spiking interneurons ($n = 31$; Supplementary Fig. 3a,b; Supplementary Table 1) with post hoc morphological reconstruction and PV/MBP immunofluorescence labeling in mPFC, S1, and CA1 (Fig. 3a,b; Supplementary Video 2). Consistent with
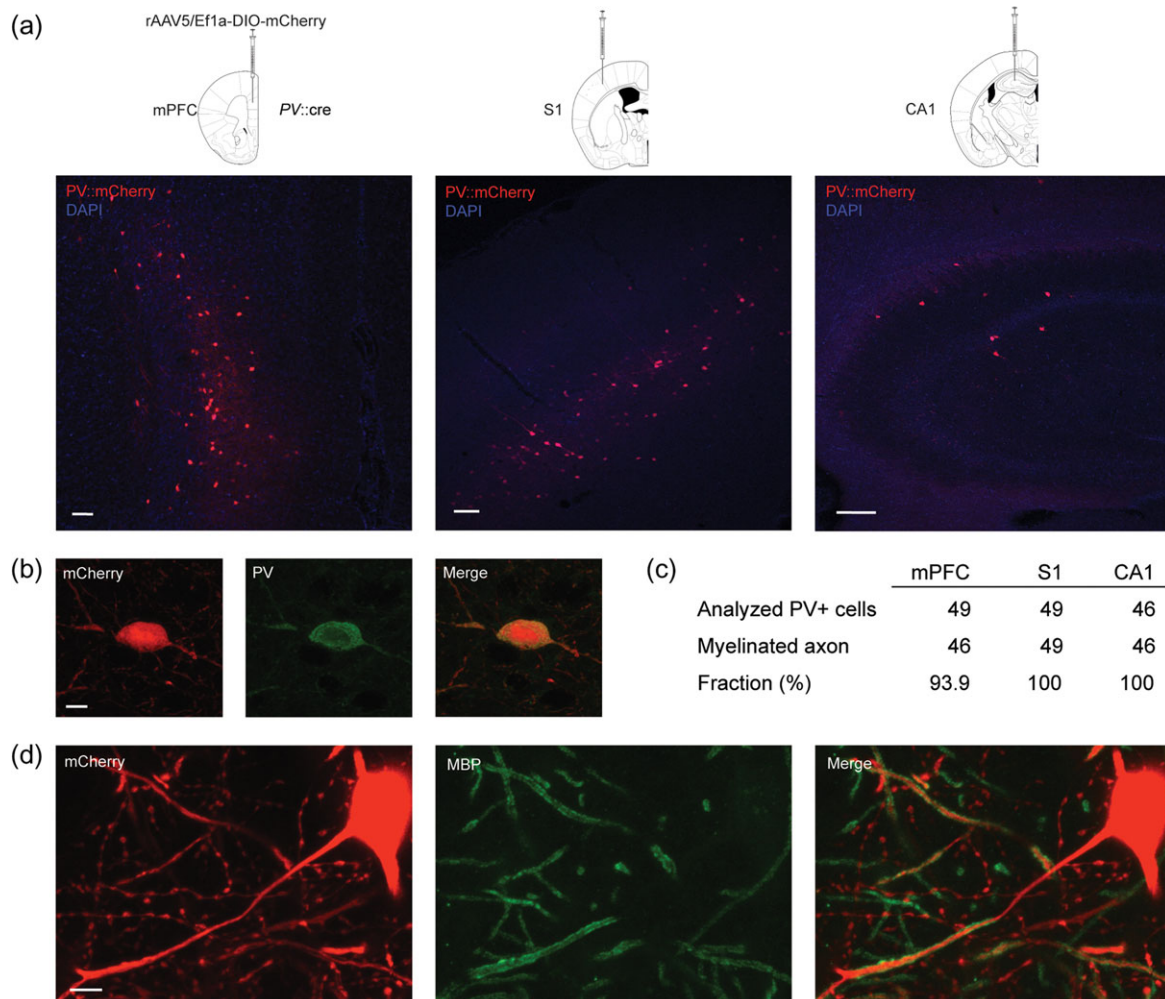

Figure 2 PV$^+$ interneurons frequently exhibit axonal myelination. (a) PV::Cre mice were injected with rAAV5/Ef1a-DIO-mCherry virus for PV-specific labeling, and sacrificed 4 weeks later. Low-magnification confocal images of PV::cre mice (representative images of $n = 7$) with virally labeled PV$^+$ cells (mCherry; red) in mPFC, S1 and hippocampal CA1. DAPI (blue) is shown for orientation. Scale bars, 100 μm. (b) Representative colocalization between mCherry (red) and PV (green) in S1. Scale bar, 10 μm. (c) The overwhelming majority of PV$^+$ cells in the cerebral cortex have myelinated axons. (d) Representative colocalization between an mCherry-filled axon (red) and MBP (green), demonstrating a myelinated axonal segment. Scale bar, 5 μm.

the results obtained with sparse viral labeling, we found that 30 of the 31 reconstructed fast-spiking PV^{+} cells exhibited myelination (total: 96.8%; mPFC: 10/11 cells [90.9%], S1:11/11 cells [100%], CA1:9/9 cells [100%]; Fig. 3c,d). Notably, PV[+] interneurons were myelinated irrespective of whether their axons originated from the soma or primary dendrite.

Reconstruction of biocytin-labeled cells allowed for classification by axonal and dendritic morphology (Supplementary Fig. 4a,b). In mPFC, 11 out of 11 PV^{+} cells were morphologically identified as basket cells (100%). Of the 11 reconstructed cells in S1, 7 cells had a basket cell morphology (63.6%), one had a basket cell morphology with large horizontally extending axons and dendrites (horizontally elongated cell; Jiang et al. 2015) (9.1%), and 3 had a shrub cell morphology (Jiang et al. 2015) (27.3%). In CA1, we found 3 distinct morphological subtypes of PV^{+} cells: 4 of the 9 reconstructed cells had a bistratified
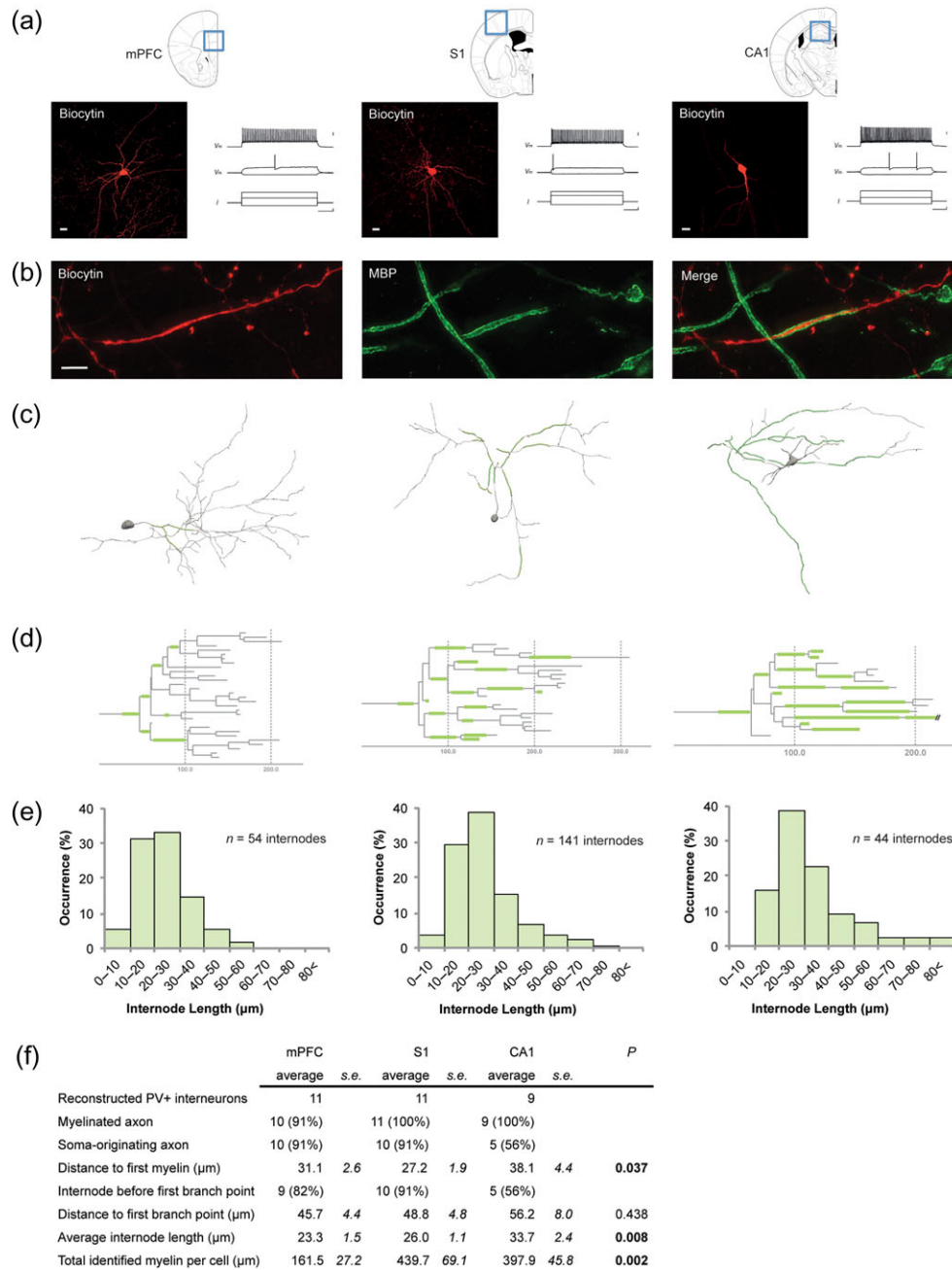

Figure 3. Topography and regional variation of PV[+] interneuron myelination. (a) Maximum projection confocal images of representative biocytin-filled PV^{+} cells (red) with a corresponding fast-spiking AP train in mPFC (left), S1 (center) and CA1 (right). Scale bars for electrophysiological traces are 20 mV, 100 ms, and 100 pA from top to bottom, respectively. (b) High-resolution SIM colocalization between a biocytin-labeled axon (red) and MBP (green), demonstrating a myelinated axonal segment. Scale bar, 10 μm. (c) Partial reconstructions of representative PV^{+} cells in mPFC, S1 and CA1. Soma and axon are shown in gray, and myelinated internodes are shown in green. Note the proximal onset and interspersed branch points between internodes. Dendrites have been removed to facilitate axonal visualization. Note the dendrite-originating axon in the right panel. (d) Axonal dendrograms showing the corresponding schematic myelin localization for each cell in (c). Axon in gray, myelin in green. Horizontal axis, μm. (e) Histogram of internode length per region (mPFC: n = 54 internodes, 10 cells; S1: n = 141 internodes, 11 cells; CA1: n = 44 internodes, 9 cells). (f) Regional characteristics of PV[+] axonal myelination. P-values are based on a one-way analysis of variance.

morphology with an axon predominantly innervating stratum oriens and radiatum (44.4%), while another 4 cells had a perisomatic morphology primarily innervating the pyramidal cell layer (44.4%). The final cell had chandelier morphology (11.1%), with distinct axo-axonic bouton cartridges originating in stratum oriens and directed orthogonally towards the pyramidal cell layer. These findings suggest that PV$^+$ interneuron myelination extends beyond the classical basket cell to include a variety of morphological subtypes.

Detailed axonal reconstructions including myelination (Fig. 3c,d; Supplementary Fig. 4c, Supplementary Fig. 5) revealed that PV$^+$ interneuron myelination was disproportionately located on proximal axonal segments. The proximal beginning of the first internode was found an average distance of 31.4 μm from the origin of the axon (mPFC: 31.1 ± 2.1 μm; S1: 27.2 ± 1.9 μm; CA1: 38.1 ± 4.4 μm), and typically occurred before the first axonal branch point (mPFC: 81.8%; S1: 90.9%; CA1: 56.6%) located at an average distance of 49.8 μm from the soma (mPFC: 45.7 ± 4.4 μm; S1: 48.8 ± 4.8 μm; CA1: 56.2 ± 8.0 μm). One cell in the mPFC had an atypical topography of myelination, in which no internodes were found until immediately distal to the secondary axonal branch points (Supplementary Fig. 6).

Overall, internodes of PV$^+$ interneurons had an average length of 27.2 μm, which varied significantly between regions (mPFC: 23.3 ± 1.5 μm, n = 54 internodes; S1: 26.0 ± 1.1 μm, n = 141; CA1: 33.7 ± 2.4 μm, n = 44; P = 0.008), with similarly right-skewed distributions (Fig. 3e). The mean total identified length of axonal myelination was 332.2 μm per cell, which varied significantly across brain regions (mPFC: 161.5 ± 27.2 μm; S1: 439.7 ± 69.1 μm; CA1: 397.9 ± 45.8 μm; P = 0.002, Fig. 3f). On average, we identified ~12 internodes per cell (mPFC: 6.6 ± 0.7 internodes per cell; S1: 14.7 ± 2.2 internodes per cell; CA1: 13.0 ± 1.6 internodes per cell). Similar to earlier findings (Schain et al. 2014), we very rarely observed myelination of branch points (Supplementary Fig. 3c).

To confirm whether myelin integrity may have been compromised during the whole-cell patch-clamp tissue preparation, we compared internodes from the in vivo viral labeling experiments (Fig. 2) with those obtained from the reconstructions following intracellular biocytin labeling (Fig. 3). No differences in any region were observed between methods (Supplementary Table 2), thereby providing an independent replication of the results and a validation of the 2 distinct methodologies for quantifying internode segments.

PV$^+$ Axons are Frequently Myelinated in the Human Brain

Next, we examined whether myelination of fast-spiking PV$^+$ interneurons extends to humans. Ex vivo whole-cell patch-clamp recording and intracellular biocytin labeling was performed in acutely resected neocortex obtained from patients undergoing surgery for subcortical tumors (n = 13 cells, 3 donors; Fig. 4). Interneurons were readily categorized as fast-spiking (n = 10) or non-fast-spiking (n = 3) based on their electrophysiological profile (Fig. 4a,b; Supplementary Table 3). Human fast-spiking interneurons exhibited 2 distinct electrophysiological characteristics not observed in mouse—pronounced sag at hyperpolarizing levels and near-threshold "humps," both of which have been previously reported in ex vivo recordings from acute non-human primate tissue (Povysheva et al. 2013).

All of the human fast-spiking interneurons we examined (10/10 cells; 100%), but none of the non-fast-spiking cells (0/3 cells), exhibited myelinated axons (P = 0.003; Fig. 4e–g). Notably,

8 of the 10 fast-spiking cells (80%) but none of the non-fast-spiking cells (0/3 cells; 0%) were PV$^+$ (P = 0.035; Fig. 4c,d). Among the 8 fast-spiking PV$^+$ cells, all had a basket cell morphology. The 2 fast-spiking PV$^-$ cells included a basket cell and a double-bouquet cell. Although the absence of PV labeling in these 2 fast-spiking cells could have resulted from washout during whole-cell recordings, it is notable that a small subset of fast-spiking cells in the mouse neocortex has recently been confirmed to lack PV expression, in particular double-bouquet cells (Jiang et al. 2015). Moreover, a subset of basket cells in the neocortex of non-human primates has also been demonstrated to lack PV expression (Povysheva et al. 2008).

Similar to our findings in mice, fast-spiking interneuron myelination in human neocortex was biased towards proximal axonal segments, beginning on average at 26.5 ± 1.4 μm from the soma (Fig. 4f,g; Supplementary Fig. 7) and most commonly occurring before the first branch point (80%) located 47.9 ± 8.2 μm from the soma. Internodes had an average length of 33.0 ± 1.4 μm (n = 194; Fig. 4h). The total length of identified axonal myelination per cell was 1035.3 ± 264.4 μm, which was notably longer than we observed in mice. On average, we identified 31.6 ± 2.5 internodes per human fast-spiking interneuron. Together, these data suggest that myelination of neocortical fast-spiking interneurons is a conserved feature of both the mouse and human brain.

PV$^+$ Axonal Branch Morphology Predicts Segmental Myelination

Internodes along PV$^+$ axons often ensheathed the full distance between branch points. However, interbranch segments were frequently unmyelinated, particularly those of shorter length (Fig 3c,d). Given the relatively small proportion of internodes <10 μm in length (Fig. 3e), we hypothesized that segmental myelination might be correlated with interbranch distance. To examine this directly, we quantified interbranch point distances up to fifth-order axonal segments and whether each corresponding segment contained an internode (Fig. 5a). In line with our hypothesis, we found that unmyelinated interbranch point segments were consistently shorter than corresponding myelinated segments (P < 0.001 for mPFC, S1, and CA1; Fig. 5b). Overall, the majority (66.7%) of interbranch segments ≥15 μm showed myelination, while interbranch segments <15 μm tended to be unmyelinated (90.8%). An analogous dichotomy was evident also in the location of the first axonal branch point, which was located closer to the soma when it arose before, compared to after, the first internode (P = 0.010). Together, this suggests that the likelihood of segmental myelination might be governed by spatial limitations imposed by axonal morphology.

Myelination Regulates the Density of PV$^+$ Axonal En Passant Boutons

We observed that the most proximal en passant boutons were frequently positioned just a short distance beyond the distal end of myelination. Moreover, the one unmyelinated mPFC basket cell that we identified using confocal imaging showed a higher density and proximally shifted topography of en passant boutons (Supplementary Fig. 8). Consequently, we hypothesized that en passant bouton formation might be constrained by myelination. To examine this possibility directly, we quantified the density of proximal en passant boutons along PV$^+$ interneuron axons in mPFC of myelin-deficient *Shiverer* mice (Fig. 6a, Supplementary Fig. 9). Using SIM imaging of intracellular biocytin-labelled fast-spiking PV$^+$ interneurons (Fig. 6b,c), we
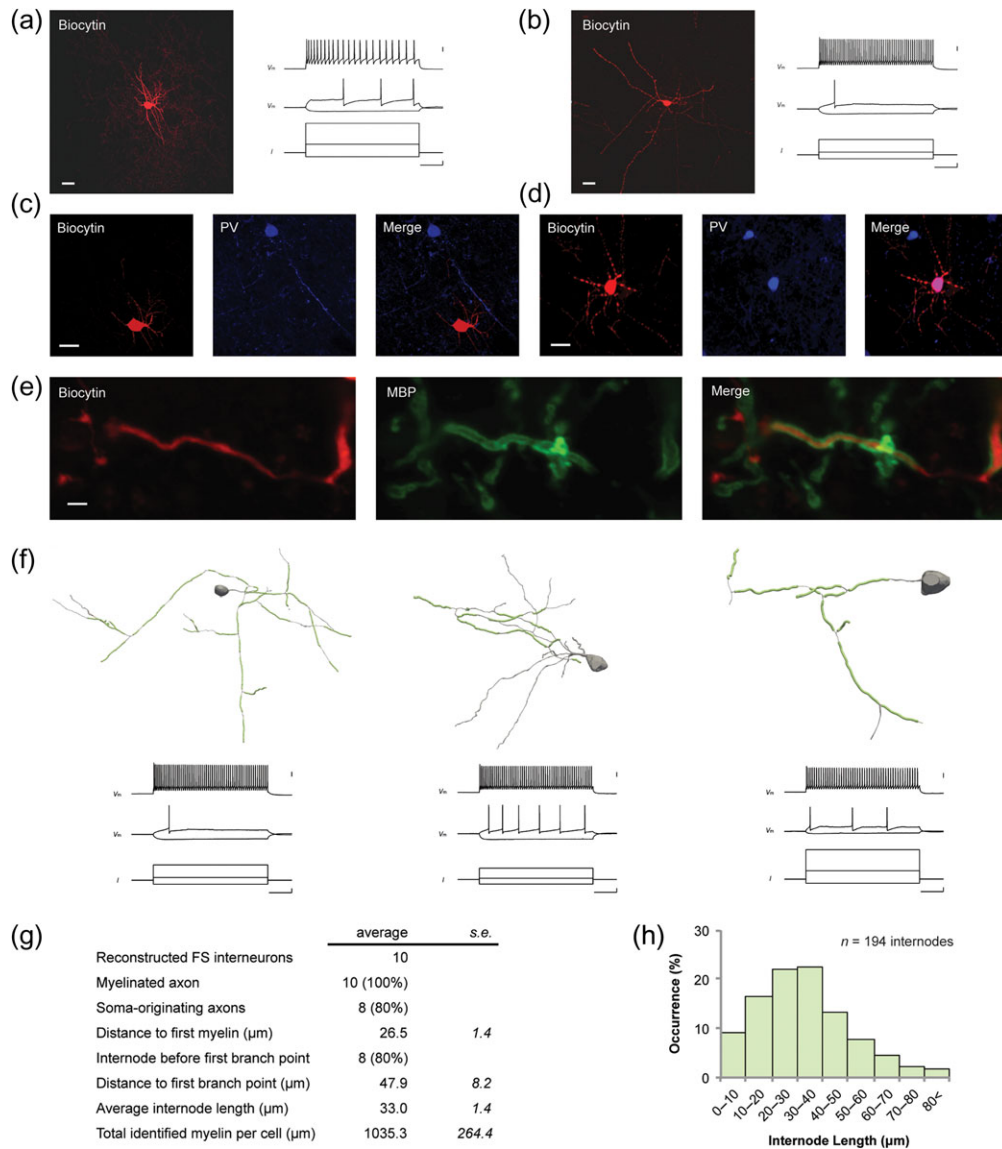
Figure 4. Fast-spiking PV$^+$ interneurons are frequently myelinated in human brain. Maximum projection confocal images of (*a*) non-fast-spiking and (*b*) fast-spiking biocytin-filled cells (red) from resected human surgical tissue. Scale bars, 15 µm. Representative voltage responses to depolarizing and hyperpolarizing current injections. Fast-spiking cells exhibited a typical suprathreshold high frequency nonadapting firing pattern. Biocytin-labeled cells (red) were classified as PV$^-$ (*c*) or PV$^+$ (*d*) on the basis of the absence or presence of colocalization with PV (blue). Scale bars, 20 µm. (*e*) Representative colocalization between biocytin-filled axons (red) and MBP (green), showing a myelinated axonal segment. Scale bar, 5 µm. (*f*) Representative examples of partially reconstructed PV$^+$ interneurons. Soma and axon are shown in gray, and myelinated internodes are shown in green. Note the proximal onset and interspersed unmyelinated branch points between internodes. Dendrites were removed from the left and right panels to facilitate axonal visualization. Note the dendrite-originating axon in the middle panel. Corresponding fast-spiking electrophysiological profiles are shown directly below each morphological reconstruction. (*g*) Characteristics of human fast-spiking interneuron axonal myelination. FS, fast-spiking. (*h*) Histogram of internode length (*n* = 194 internodes, 10 cells). Scale bars for electrophysiological traces in a, b and f are 20 mV, 100 pA and 100 ms from top to bottom, respectively.

observed a more proximal onset (*P* < 0.001; *Shiverer*: 47.4 ± 5.7 µm from soma; WT: 111.1 µm ± 7.7 from soma; Fig. 6*d*) and higher density (*P* = 0.013; *Shiverer*: 3.3 ± 0.7 boutons per 100 µm; WT: 0.7 ± 0.5 boutons per 100 µm; Fig. 6*e*) of en passant boutons in the absence of myelination. However, axonal length was unchanged (*P* = 0.827; *Shiverer*: 137.8 ± 6.9 µm; WT: 139.9 ± 5.5 µm; Fig. 6*f*). Together, these findings suggest that myelination regulates the density of PV$^+$ axonal en passant boutons and offer additional support for a broad interrelationship between axonal morphology and myelination.

Discussion

In the present paper, we report that a substantial fraction of myelin in the cerebral cortex ensheaths axons of GABAergic interneurons, a finding predominately attributable to the fast-spiking PV$^+$ subclass of interneurons. Moreover, utilizing 2 independent methodologies, we find that a high proportion of fast-spiking PV$^+$ interneurons in mouse cerebral cortex exhibit axonal myelination. In addition, using ex vivo whole-cell recordings and intracellular biocytin labeling of human neocortex, we confirm that fast-spiking PV$^+$ cells in the human brain are
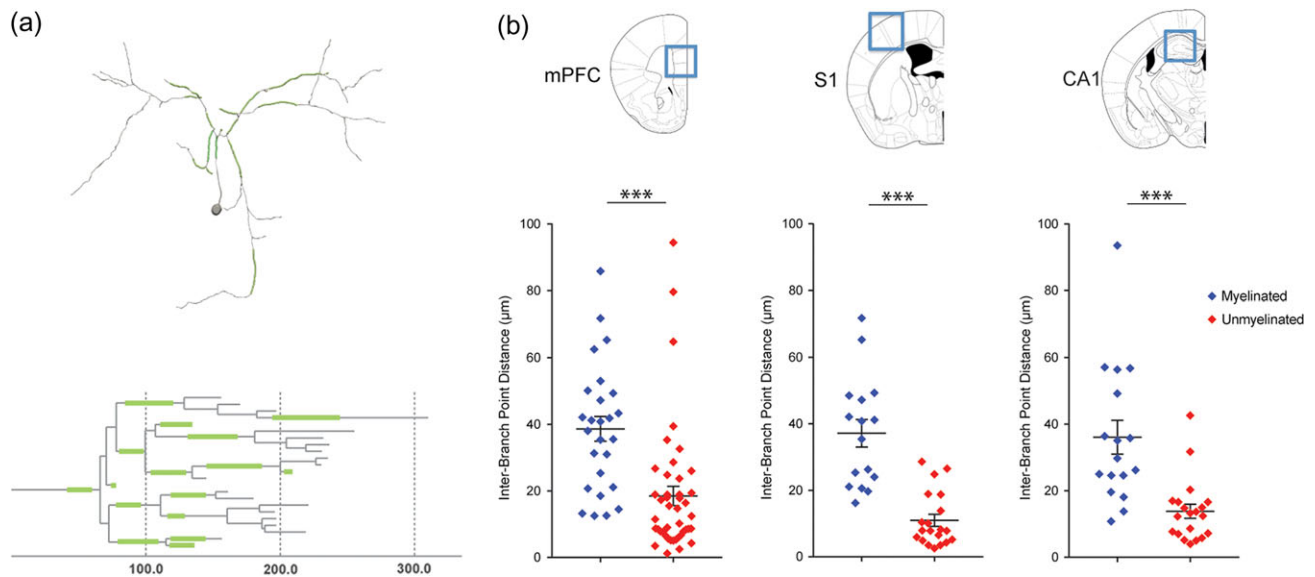
Figure 5. Axonal morphology predicts segmental myelination. (*a*) Representative PV[+] interneuron reconstruction (top) from S1, along with its axonal dendrogram (bottom) with myelinated segments shown in green. Dendrites were removed to facilitate axonal visualization. Horizontal axis, μm. (*b*) Quantification of interbranch point distances (second to fifth-order axonal branches) for myelinated versus unmyelinated segments in mPFC (left), S1 (middle), and CA1 (right). Myelinated segments (blue) are significantly longer than unmyelinated segments (red) in all 3 regions. *n* = 4 cells per region. ***P < 0.001; Student's *t*-test

also frequently myelinated. PV[+] interneuron myelination most commonly involves the proximal axon, consists of internodes interspersed by axonal branch points, and occurs predominantly on longer interbranch segments. Finally, and suggestive of a causal functional influence of myelination on PV[+] axonal morphology, we find that myelin-deficient *Shiverer* mice exhibit an increased density and ectopic localization of en passant boutons.

A recent study (Micheva et al. 2016) reported a large contribution of GABAergic interneurons to the total myelin content of primary somatosensory cortex using array tomography and scanning electron microscopy. Our findings considerably extend these results by demonstrating that the contribution of GABAergic interneuron myelination is region-dependent, with the mPFC exhibiting a lower, and the hippocampus a higher, relative fraction of interneuron myelination. In the CA1 subregion of the hippocampus, nearly 80% of myelin in stratum pyramidale and radiatum originates from GABAergic interneurons, which is contributed almost exclusively by PV[+] interneurons. This finding could suggest a particularly important contribution of interneuron myelination in hippocampal function. Alternatively, the high proportion of myelin contributed by GABAergic interneurons may simply reflect the limited myelination of CA1 pyramidal neurons. Regardless, in light of the predominant contribution of interneuron myelination to the total myelin content of the hippocampus, experience-dependent or neuropathological alterations of hippocampal myelination are likely to involve PV[+] interneurons. Conversely, the relatively lower contribution of interneuron myelination in the prefrontal versus somatosensory cortex is at least in part, if not entirely, due to a more limited extent of myelination per PV[+] interneuron. Notably however, our analysis was performed entirely during early adulthood for which it remains unknown whether the relative contribution of cerebral cortex interneuron myelination is neurodevelopmentally regulated.

In addition to PV[+] interneuron myelination, we also find a small, but consistent, contribution of cortical myelin arising from axons of SOM[+] interneurons. The contribution of SOM[+] interneuron myelination is similar in mPFC and S1, but somewhat higher in CA1 consistent with the limited myelination of hippocampal principal cells (Debanne et al. 2011). SOM[+] interneurons are a heterogeneous group of GABAergic cells with relatively lower firing rates than PV[+] interneurons (Urban-Ciecko and Barth 2016). A precise quantification of the proportion of SOM[+] interneurons that are myelinated, and whether they exhibit a similarly biased topography of proximal myelination as PV^{+} cells, remains to be determined.

Although the majority of our PV[+] interneuron reconstructions exhibited a basket cell morphology, we also recovered fast-spiking PV[+] bistratified, shrub, and chandelier cells in the CA1 subregion of the hippocampus, all of which had myelinated axons. Although these observations require further replication to be considered conclusive, they nevertheless suggest that PV[+] interneuron myelination is likely to extend beyond the classical basket cell subtype. Moreover, they also highlight the question of whether each PV[+] interneuron subtype has distinct aspects of their topography and function of axonal myelination.

Using axonal reconstructions, we find that PV[+] interneuron myelination has a spatially biased topography with internodes occurring predominantly on axonal segments of low branch order. In particular, the first internode is typically positioned ~30 μm from the soma, directly following the location of AP initiation (~25 μm from the soma) within the axon initial segment (Hu and Jonas 2014; Li et al. 2014). Interestingly, none of the cells showed exceptionally long distances to myelin onset (>60 μm), as has recently been shown for a subset of S1 pyramidal cells (Tomassy et al. 2014). In most instances, the first axonal branch point occurs immediately following the first internode at ~45 μm from the soma. This stereotyped sequence of axon initial segment—internode—branch point raises the question of whether the first internode and branch point function to modulate AP generation in PV[+] interneurons, as has been previously suggested for cerebellar Purkinje cells (Clark et al. 2005) and S1 layer V pyramidal cells (Hamada and Kole 2015).

Low-order axonal branches of PV[+] interneurons contain myelinated and unmyelinated segments interspersed with
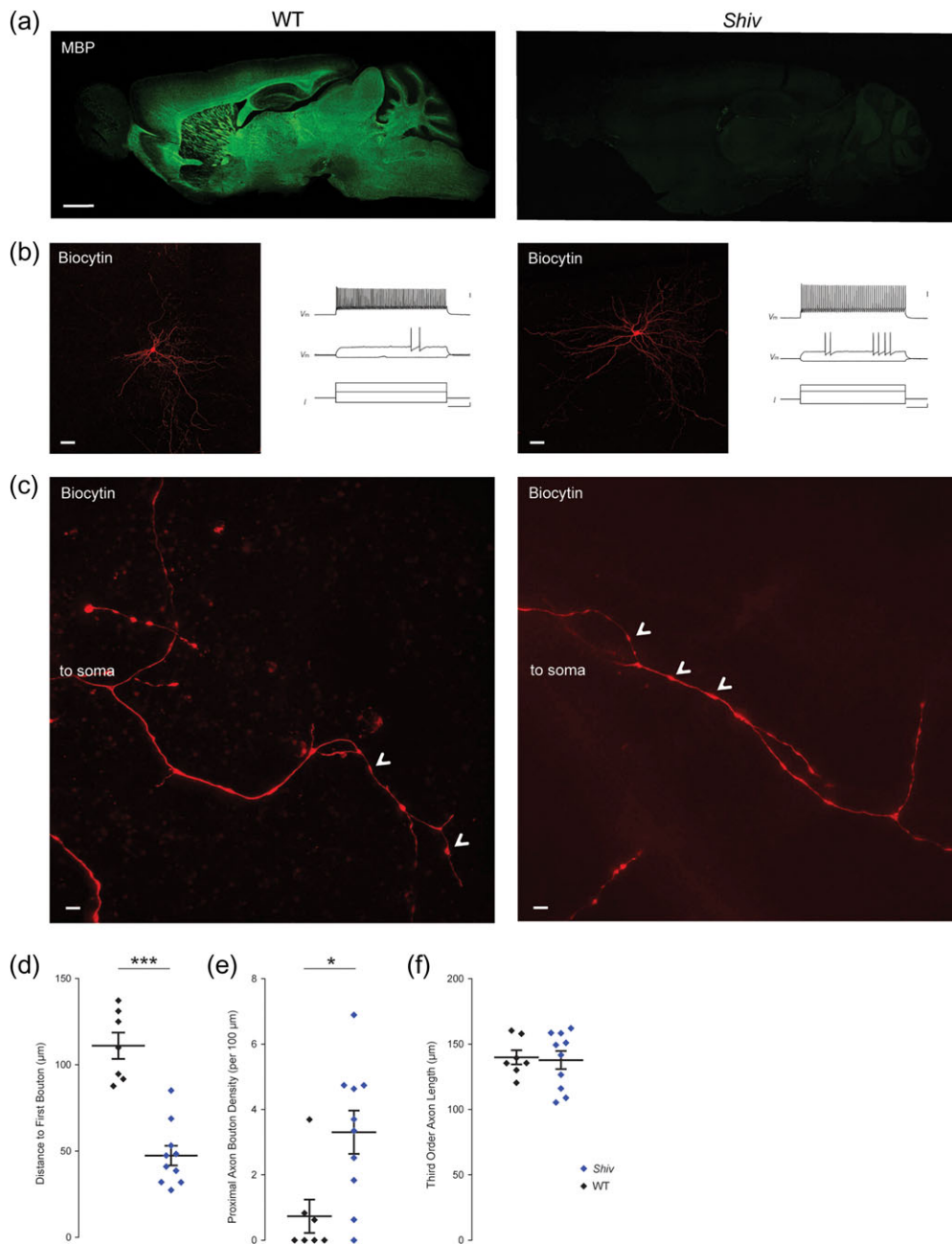
Figure 6. Altered PV[+] axon morphology in myelin-deficient *Shiverer* mice. (*a*) Mid-sagittal section from *Shiverer* mice (*Shiv*) demonstrates the absence of MBP expression, whereas WT mice show extensive myelination (green). Scale bar, 1 mm. (*b*) Maximum projection confocal images of representative biocytin-filled PV^{+} cells (red) from the mPFC with a corresponding fast-spiking AP train in *Shiverer* (right) and WT (left) littermates. Scale bars are 20 mV, 100 ms, and 100 pA from top to bottom, respectively. (*c*) High-resolution SIM images of biocytin-labeled axons, centered on the third branch order, showing morphological evidence of en passant boutons (arrowheads) in *Shiv* (left) and WT (right). Scale bar, 10 μm. (*d*) *Shiv* mice (blue) have a significantly more proximal bouton onset, and (*e*) higher density of boutons along the proximal axon compared to WT mice (red). (*f*) Cumulative axonal length (through third-order axon branches) is unchanged (P = 0.827). *Shiverer*: n = 10 cells; WT: n = 7 cells. Bars represent mean ± SEM. ***P < 0.001; *P = 0.013; Student's t-test.

branch points. Notably, we observed a correlation between the interbranch distance and the probability of that segment being myelinated, in which axonal segments connecting branch points in close proximity were less likely to contain internodes. Given that the smallest observed internode length was ~10 μm, there appears to be a critical threshold distance of uninterrupted axon required for an internode to be stably established, beyond which shorter axonal segments remain unmyelinated. Notably, this mechanism could also account for the high

proportion of PV[+] interneurons that have their first internode located proximal to the first axonal branch point.

The functional significance of cerebral cortex interneuron myelination remains at present largely unknown. Considering that mouse cerebral cortex PV[+] interneurons exhibit a total axonal length of ~20 to 30 mm (Hu et al. 2014; see also Supplementary Fig 4c), only ~1–2% of the total axonal length is myelinated. Notably however, the proximally biased distribution of internodes along PV[+] interneuron axons observed

consistently in both mouse and human might be an efficient mechanism to ensure that a high proportion of APs pass through myelinated segments, thereby potentially enhancing conduction velocity, fidelity and metabolic support. In addition, the most distally located internodes were nearly always followed by morphological evidence of en passant boutons, raising the question of whether myelination is functionally related to the establishment and/or maintenance of boutons. Therefore, we examined myelin-deficient *Shiverer* mice and indeed found that in the absence of myelin, the proximal axon exhibited a higher density and proximally ectopic localization of en passant boutons. Accordingly, PV⁺ interneuron axonal myelination might function in part to inhibit synapse formation along the proximal axon. By limiting synapse formation on the proximal axon, myelination could facilitate PV⁺ interneurons in achieving synchronous inhibition of their postsynaptic targets, given that en passant boutons have been suggested to attenuate axonal conduction velocity ([Hu and Jonas 2014](#)). Therefore, in addition to facilitating AP propagation through the classical mechanisms mediated by increased axonal diameter and membrane resistance, myelin may also function to enhance conduction velocity by limiting synapse formation along the proximal axon.

Compared to glutamatergic pyramidal neurons, the relatively short conduction delays observed in PV⁺ interneurons are thought to result from their faster membrane time constant, lower AP threshold, and small aspiny dendritic morphology ([Brown et al. 1981](#); [McCormick et al. 1985](#); [Lacaille et al. 1987](#); [Beaulieu et al. 1992](#); [Buonomano 2000](#); [Hu et al. 2014](#)). Moreover, PV⁺ interneurons are highly energy demanding ([Kann et al. 2014](#)), for which myelin provides axonal metabolic support ([Fünfschilling et al. 2012](#); [Lee et al. 2012b](#); [Saab et al. 2016](#)). However, more distal myelination of PV⁺ interneurons might be limited by the apparently strict biophysical threshold of a minimum caliber (~300 nm) for oligodendrocytes to successfully ensheath axonal segments ([Lee et al. 2012a](#)). Spatially restricted proximal myelination of fast-spiking PV⁺ interneurons might therefore be an efficient mechanism to enhance conduction velocity, AP fidelity and metabolic support, while also limiting the formation of lower conductivity en passant synapses, together in the service of coordinating rapid, temporally synchronous GABA release across the entire axonal tree.

An interesting outstanding question is whether direct synaptic contacts from PV⁺ interneurons onto oligodendrocyte precursor cells regulate interneuron myelination ([Orduz et al. 2015](#)), and how their intercellular interactions during early waves of neural migration might shape interneuron myelination ([Voronova et al. 2017](#)). Especially interesting is the possible relevance of how the distance-dependence of the contact between oligodendrocyte progenitor cells and PV⁺ interneurons ([Orduz et al. 2015](#)) might be related to the proximally biased topography of PV⁺ interneuron myelination. Moreover, the recent demonstration of a wide diversity of myelinating oligodendrocyte subtypes classified by single-cell RNA sequencing raises the question of whether individual oligodendrocytes have constraints in the repertoire of neuronal cell types that they are capable of ensheathing ([Marques et al. 2016](#)). Furthermore, recent studies demonstrating that axonal myelination of pyramidal neurons is highly dynamic and experience-dependent ([Gibson et al. 2014](#)) also raise the question of the extent to which interneuron myelination has similar, or perhaps distinct, mechanisms of developmental and experience-dependent plasticity.

Using acute surgically resected tissue, we also confirmed that interneuron myelination extends to the human neocortex, with quantitative parameters largely similar to mouse neocortex. This is particularly notable given that our findings might have been influenced by factors not present in rodent studies, such as advanced age, confounding by surgical indication, or medication. Given the putative role of both GABAergic interneurons and myelination in disorders of the brain, the confirmation of PV⁺ interneuron myelination in the human neocortex provides additional support for its potential pathophysiological relevance.

In summary, we find that PV⁺ interneurons in the mouse and human cerebral cortex are frequently myelinated. Internodes along PV⁺ interneuron axons have a spatially biased proximal topography, are correlated with axonal morphology, and exhibit quantitative differences between cortical subregions. Moreover, we demonstrate that in the absence of myelin, PV⁺ interneurons acquire a higher density and proximally ectopic localization of en passant boutons. Together, these findings suggest that myelination is an important feature governing the function of cerebral cortex interneurons.

Supplementary Material

Supplementary data are available at *Cerebral Cortex* online.

Funding

Notes

Conflict of Interest: None declared.

References

Barysheva M, Jahanshad N, Foland-Ross L, Altshuler LL, Thompson PM. 2013. White matter microstructural abnormalities in bipolar disorder: A whole brain diffusion tensor imaging study. NeuroImage Clin. 2:558–568.

Beaulieu C, Dyck R, Cynader M. 1992. Enrichment of glutamate in zinc-containing terminals of the cat visual cortex. Neuroreport. 3:861–864.

Brown DA, Higgins AJ, Marsh S, Smart TG. 1981. Actions of GABA on mammalian neurones, axons, and nerve terminals. Adv Biochem Psychopharmacol. 29:321–326.

Buonomano DV. 2000. Decoding temporal information: a model based on short-term synaptic plasticity. J Neurosci. 20:1129–1141.

Chernoff GF. 1981. Shiverer: an autosomal recessive mutant mouse with myelin deficiency. J Hered. 72:128.

Clark BA, Monsivais P, Branco T, London M, Häusser M. 2005. The site of action potential initiation in cerebellar Purkinje neurons. Nat Neurosci. 8:137–139.

Debanne D, Campanac E, Bialowas A, Carlier E, Alcaraz G. 2011. Axon physiology. Physiol Rev. 91:555–602.

Fünfschilling U, Supplie LM, Mahad D, Boretius S, Saab AS, Edgar J, Brinkmann BG, Kassmann CM, Tzvetanova ID, Möbius W, et al. 2012. Glycolytic oligodendrocytes maintain myelin and long-term axonal integrity. Nature. 485:517–521.

Gibson EM, Purger D, Mount CW, Andrea K, Lin GL, Wood LS, Inema I, Miller SE, Bieri G, Zuchero JB, et al. 2014. Neuronal activity promotes oligodendrogenesis and adaptive myelination in the mammalian brain. Science. 344(6183):1252304.

Hamada MS, Kole MHP. 2015. Myelin loss and axonal ion channel adaptations associated with gray matter neuronal hyperexcitability. J Neurosci. 35:7272–7286.

Hippenmeyer S, Vrieseling E, Sigrist M, Portmann T, Laengle C, Ladle DR, Arber S. 2005. A developmental switch in the response of DRG neurons to ETS transcription factor signaling. PLoS Biol. 3:e159.

Hu H, Cavendish JZ, Agmon A. 2013. Not all that glitters is gold: off-target recombination in the somatostatin-IRES-Cre mouse line labels a subset of fast-spiking interneurons. Front. Neural Circuits. 7:195.

Hu H, Gan J, Jonas P. 2014. Interneurons. Fast-spiking, parvalbumin⁺ GABAergic interneurons: from cellular design to microcircuit function. Science. 345:1255263.

Hu H, Jonas P. 2014. A supercritical density of Na(+) channels ensures fast signaling in GABAergic interneuron axons. Nat Neurosci. 17:686–693.

Jiang X, Shen S, Cadwell CR, Berens P, Sinz F, Ecker AS, Patel S, Tolias AS. 2015. Principles of connectivity among morphologically defined cell types in adult neocortex. Science. 350:aac9462–aac9462.

Kann O, Papageorgiou IE, Draguhn A. 2014. Highly energized inhibitory interneurons are a central element for information processing in cortical networks. J Cereb Blood Flow Metab. 34:1270–1282.

Kumar J, Iwabuchi S, Oowise S, Balain V, Palaniyappan L, Liddle PF. 2015. Shared white-matter dysconnectivity in schizophrenia and bipolar disorder with psychosis. Psychol Med. 45:759–770.

Lacaille JC, Mueller AL, Kunkel DD, Schwartzkroin PA. 1987. Local circuit interactions between oriens/alveus interneurons and CA1 pyramidal cells in hippocampal slices: electrophysiology and morphology. J Neurosci. 7:1979–1993.

Lee S, Leach MK, Redmond SA, Chong SYC, Mellon SH, Tuck SJ, Feng Z, Corey JM, Chan JR. 2012a. A culture system to study oligodendrocyte myelination processes using engineered nanofibers. Nat Methods. 9:917–922.

Lee Y, Morrison BM, Li Y, Lengacher S, Farah MH, Hoffman PN, Liu Y, Tsingalia A, Jin L, Zhang P-W, et al. 2012b. Oligodendroglia metabolically support axons and contribute to neurodegeneration. Nature. 487:443–448.

Li T, Tian C, Scalmani P, Frassoni C, Mantegazza M, Wang Y, Yang M, Wu S, Shu Y. 2014. Action potential initiation in neocortical inhibitory interneurons. PLoS Biol. 12:e1001944.

Liu J, Dietz K, DeLoyht JM, Pedre X, Kelkar D, Kaur J, Vialou V, Lobo MK, Dietz DM, Nestler EJ, et al. 2012. Impaired adult myelination in the prefrontal cortex of socially isolated mice. Nat Neurosci. 15:1621–1623.

Madisen L, Mao T, Koch H, Zhuo J, Berenyi A, Fujisawa S, Hsu Y-WA, Garcia AJ, Gu X, Zanella S, et al. 2012. A toolbox of Cre-dependent optogenetic transgenic mice for light-induced activation and silencing. Nat Neurosci. 15:793–802.

Makinodan M, Rosen KM, Ito S, Corfas G. 2012. A critical period for social experience-dependent oligodendrocyte maturation and myelination. Science. 337:1357–1360.

Marín O. 2012. Interneuron dysfunction in psychiatric disorders. Nat Rev Neurosci. 13:107–120.

Marques S, Zeisel A, Codeluppi S, van Bruggen D, Mendanha Falcão A, Xiao L, Li H, Häring M, Hochgerner H, Romanov RA, et al. 2016. Oligodendrocyte heterogeneity in the mouse juvenile and adult central nervous system. Science. 352:1326–1329.

McCormick DA, Connors BW, Lighthall JW, Prince DA. 1985. Comparative electrophysiology of pyramidal and sparsely spiny stellate neurons of the neocortex. J Neurophysiol. 54:782–806.

McGee AW, Yang Y, Fischer QS, Daw NW, Strittmatter SM. 2005. Experience-driven plasticity of visual cortex limited by myelin and Nogo receptor. Science. 309:2222–2226.

Micheva KD, Wolman D, Mensh BD, Pax E, Buchanan J, Smith SJ, Bock DD. 2016. A large fraction of neocortical myelin ensheaths axons of local inhibitory neurons. Elife. 5:e15784.

Müller C, Remy S. 2014. Dendritic inhibition mediated by O-LM and bistratified interneurons in the hippocampus. Front. Synaptic Neurosci. 6:23.

Nave K-A, Werner HB. 2014. Myelination of the nervous system: mechanisms and functions. Annu Rev Cell Dev Biol. 30:503–533.

Orduz D, Maldonado PP, Balia M, Vélez-Fort M, de Sars V, Yanagawa Y, Emiliani V, Angulo MC. 2015. Interneurons and oligodendrocyte progenitors form a structured synaptic network in the developing neocortex. Elife. 4:1–20.

Pala A, Petersen CCH. 2015. In vivo measurement of cell-type-specific synaptic connectivity and synaptic transmission in layer 2/3 mouse barrel cortex. Neuron. 85:68–75.

Povysheva NV, Zaitsev AV, Rotaru DC, Gonzalez-Burgos G, Lewis DA, Krimer LS. 2008. Parvalbumin-positive basket interneurons in monkey and rat prefrontal cortex. J Neurophysiol. 100:2348–2360.

Povysheva NV, Zaitsev AV, Gonzalez-Burgos G, Lewis DA. 2013. Electrophysiological heterogeneity of fast-spiking interneurons: chandelier versus basket cells. PLoS One. 8:e70553.

Rane P, Cochran D, Hodge SM, Haselgrove C, Kennedy DN, Frazier JA. 2015. Connectivity in autism: a review of MRI connectivity studies. Harv Rev Psychiatry. 23:223–244.

Saab AS, Tzvetavona ID, Trevisiol A, Baltan S, Dibaj P, Kusch K, Möbius W, Goetze B, Jahn HM, Huang W, et al. 2016. Oligodendroglial NMDA receptors regulate glucose import and axonal energy metabolism. Neuron. 91:119–132.

Schain AJ, Hill RA, Grutzendler J. 2014. Label-free in vivo imaging of myelinated axons in health and disease with spectral confocal reflectance microscopy. Nat Med. 20:443–449.

Stedehouder J, Kushner SA. 2017. Myelination of parvalbumin interneurons: a parsimonious locus of pathophysiological convergence in schizophrenia. Mol Psychiatry. 22(1):4–12.

Taniguchi H, He M, Wu P, Kim S, Paik R, Sugino K, Kvitsiani D, Kvitsani D, Fu Y, Lu J, et al. 2011. A resource of Cre driver lines for genetic targeting of GABAergic neurons in cerebral cortex. Neuron. 71:995–1013.

Tomassy GS, Berger DR, Chen H-H, Kasthuri N, Hayworth KJ, Vercelli A, Seung HS, Lichtman JW, Arlotta P. 2014. Distinct profiles of myelin distribution along single axons of pyramidal neurons in the neocortex. Science. 344:319–324.

Urban-Ciecko J, Barth AL. 2016. Somatostatin-expressing neurons in cortical networks. Nat Rev Neurosci. 17:401–409.

Voronova A, Yuzwa SA, Wang BS, Zahr S, Syal C, Wang J, Kaplan DR, Miller FD. 2017. Migrating interneurons secrete fractalkine to promote oligodendrocyte formation in the developing mammalian brain. Neuron. 94:500–516.e9.

White T, Ehrlich S, Ho B-C, Manoach DS, Caprihan A, Schulz SC, Andreasen NC, Gollub RL, Calhoun VD, Magnotta VA. 2013. Spatial characteristics of white matter abnormalities in schizophrenia. Schizophr Bull. 39:1077–1086.